Colloids and Surfaces B: Biointerfaces 149 (2017) 174–183

Contents lists available at ScienceDirect

Colloids and Surfaces B: Biointerfaces

journal homepage: www.elsevier.com/locate/colsurfb

Nanomechanical properties of composite protein networks of erythroid membranes at lipid surfaces

Mario Encinar[a], Santiago Casado[b], Alicia Calzado-Martín[a], P. Natale[c,d], Álvaro San Paulo[a], Montserrat Calleja[a], Marisela Vélez[b,e], Francisco Monroy[c,d,*], Iván López-Montero[c,d,*]

[a] Instituto de Microelectrónica de Madrid, CSIC, 28760 Tres Cantos, Spain
[b] IMDEA Nanociencia, Ciudad Universitaria de Cantoblanco, 28049 Madrid, Spain
[c] Dpt. Physical Chemistry I, Universidad Complutense de Madrid, 28040 Madrid, Spain
[d] Instituto de Investigación Hospital Doce de Octubre (i+12), 28041 Madrid, Spain
[e] Instituto de Catálisis y Petroleoquímica, CSIC, Ciudad Universitaria de Cantoblanco, 28049 Madrid, Spain

ARTICLE INFO

Article history:
Received 4 April 2016
Received in revised form 11 October 2016
Accepted 12 October 2016
Available online 13 October 2016

Keywords:
Giant vesicles
Erythrocyte
Lipid membrane
Cytoskeleton reconstitution
AFM
PeakForce tapping quantitative nanomechanical mapping

ABSTRACT

Erythrocyte membranes have been particularly useful as a model for studies of membrane structure and mechanics. Native erythroid membranes can be electroformed as giant unilamellar vesicles (eGUVs). In the presence of ATP, the erythroid membrane proteins of eGUVs rearrange into protein networks at the microscale. Here, we present a detailed nanomechanical study of individual protein microfilaments forming the protein networks of eGUVs when spread on supporting surfaces. Using Peak Force tapping Atomic Force Microscopy (PF-AFM) in liquid environment we have obtained the mechanical maps of the composite lipid-protein networks supported on solid surface. In the absence of ATP, the protein pool was characterized by a Young's Modulus $E_{pool} \approx 5–15$ MPa whereas the complex filaments were found softer after protein supramolecular rearrangement; $E_{fil} \approx 0.4$ MPa. The observed protein softening and reassembling could be relevant for understanding the mechanisms of cytoskeleton reorganization found in pathological erythrocytes or erythrocytes that are affected by biological agents.

1. Introduction

Red Blood Cells (RBCs) contain a high concentration of hemoglobin, a carrier protein that transports molecular oxygen from the lungs to the tissues. During oxygen transport, RBCs undergo large stretching and shear deformations. The membrane skeleton of RBCs is a supramolecular structure that endows these cells with sufficient mechanical resilience to undergo deformation without failure in service conditions.

The native erythroid membrane is composed of lipids and a skeletal protein network. This protein network is formed by flexible spectrin filaments of 50 nm length that are cross-linked by junctional complexes [1] that contain short actin filaments (typically, 35 nm in length), which are capped by regulation proteins. Early electron microscopy (EM) studies with stretched membrane patches revealed a two-dimensional lattice made of straight spectrin filaments that intersect at the junctional complexes forming a nearly-hexagonal planar network [2,3] Immunolocalization of tropomodulin, tropomyosin and actin in spread human erythrocyte skeletons. The recent use of cryo-TEM tomography allowed the imaging of the three-dimensional structure of the RBC cytoskeleton in its intact native state [4]. Those studies show the presence of a tridimensional foam-like densely packed meshwork of entangled filaments instead of the quasi-regular 2D-lattice seen in the stretched membrane patches. Structural alteration due to the presence of mutated proteins in the network result in alterations of RBC deformability and plasticity, a common feature of numerous erythroid diseases as spherocytosis, sickle cell anemia and Fanconi's anemia among others [5–7].

The nanostructural characterisation of dry individual filaments of erythrocyte cytoskeleton became available with the development of single molecule techniques as Atomic Force Microscopy (AFM) [8–10]. Nonetheless, AFM turned out be a highly versatile tool to investigate biological membranes under physiological wet conditions [11,12]. AFM structural studies on native erythroid membranes have shown both classes of structures, well-defined polymerized networks [13,14] that resemble the topology of the regular skeleton revealed from EM and, alternatively, disordered

* Corresponding authors at: Dpt. Physical Chemistry I, Universidad Complutense de Madrid, 28040 Madrid, Spain.
E-mail addresses: monroy@quim.ucm.es (F. Monroy), ivanlopez@quim.ucm.es (I. López-Montero).

http://dx.doi.org/10.1016/j.colsurfb.2016.10.022

assemblies that are constituted by unstructured protein complexes [15,16]. Reorganization of the erythroid cytoskeleton associated to biochemical or biological factors including Ca^{2+} concentration [17,18], phosphorylation state [16], mutations in cytoskeletal proteins [19] or parasite infection [20] have been also recorded using AFM. A significant amount of network rearrangement and protein aggregation occurred under those conditions, including both increased spectrin length and mesh size. Furthermore, high-resolution force distance based atomic force microscopy allows the biophysical characterization of protein structures [21], like individual filaments of polymerizing erythroid proteins [22], and the quantitative measurement of the nano-mechanical characteristics of the cytoskeleton components, to correlate local stiffness with the phosphorylation state [16].

Microscopic spectrin networks can be artificially reconstructed on giant vesicles made of native membrane of human erythroid cells (erythroGUVs) [23]. eGUVs can adsorb onto glass cover slides for surface characterization. In this work, taking advantage of AFM combined with fluorescence microscopy imaging, we map the topology and the intrinsic stiffness of erythroid membrane skeletons supported on lipid surfaces. We have differentially unveiled the polymerization and networking of actin-spectrin composite filaments of the artificially reconstructed erythroid networks using AFM in Amplitude and Peak Force modulated modes. The superposition of topographic and nano-mechanical maps allowed us to correlate structure and mechanics of the different single filaments of the network. Our results deliver new insights to better understand the mechanism that underlies the important question of cytoskeleton organization and remodeling when erythrocytes are affected by age, disease (sickle cell anemia, diabetes) or external pathogenic agents, such as venoms [24] or parasites [25].

2. Materials and methods

2.1. Chemicals

Sodium Chloride (NaCl), Potassium chloride (KCl, 99.5%), sodium phosphate (NaH2PO4), Magnesium sulphate (MgSO4), Magnesium Chloride ($MgCl_2$), Ethylenediaminetetraacetic acid (EDTA), Adenosine-5′-triphosphate (ATP) and HEPES were supplied by Sigma-Aldrich. Glucose and sucrose were from Riedel-de Haën. Ultrapure water was taken from a Milli-Q unit (Millipore, conductivity lower than 18MΩ cm, organic residuum less than 2ppb).

2.2. Lipids, antibodies and fluorescent probes

The fluorescent lipid 1,2-dioleoyl-sn-*glycero*-3-phosphoethanolamine-*N*-(lissamine rhodamine B sulfonyl) (Rh-PE) was supplied by Avanti Polar Lipids and dissolved in chloroform at 1 mg/ml after receipt. Monoclonal anti-human spectrin (α and β) (clone SB-S1) was purchased from Sigma-Alrich. The secondary fluorescent antibody Alexa Fluor 488 goat antimouse IgG, IgA, IgM (H + L) was supplied by Invitrogen. Alexa Fluor® 594 Phalliodin (300 U) was purchased from Invitrogen and dissolved in 1.5 mL ethanol after receipt. Molecular solutions were stored at −20 °C.

2.3. Erythrocyte membrane extraxtion

Human blood was obtained from healthy donors and stored in EDTA-containing tubes to avoid coagulation. Immediately after, the erythrocyte concentrate is obtained by washing out three times in PBS buffer (1 blood/5 PBS (vol/vol); NaCl 150 mM, sodium phosphate 5 mM, pH = 8) following the Steck and Kant protocol [26]. Then, cytoplasm contents are removed under hemolytic conditions in a hypotonic buffer (1 erythroid/40 buffer (vol/vol); 1 mM MgSO4, sodium phosphate 5 mM, pH = 8). Sealed ghosts were carefully recuperated after centrifugation (22,000*g*, 10 min; 4 °C), discarding the hard button enriched in proteases obtained at the tube bottom. The buffer washing out was repeated twice again in a dilution ramp at constant pH = 8 (1st: 1 mM $MgSO_4$, sodium phosphate 2.5 mM; 2nd: 1 mM $MgSO_4$, sodium phosphate 1.25 mM) [27]. The procedure was carried out at 4 °C. The erythroid membrane is vesiculated by passing the extract suspension 5 times through a gauge needle (No. 23) using a 50 mL syringe. The final protein concentration of the erythrocyte membrane is ca. 0.5 mg/ml (see SI) as estimated by the RC DC Protein Assay kit (BIORAD) using BSA as a reference. Aliquots (20 μL) of the RBC membrane concentrate were stored at −20 °C.

2.4. ErytroGUVs preparation

Giant vesicles made of erythrocyte membrane (ErytroGUVs) were prepared by electro-swelling [28] and following the same protocol described in [22]. Prior to spreading on the electro-swelling chamber erythroid membranes were labeled with fluorescent Rho-PE. For that, erythroid membrane aliquots were incubated for 30 min in an Eppendorf tube previously containing a lipid film. These films are prepared by solvent evaporation from a chloroform solution containing 1 mg/ml of Rh-PE.

2.5. Indirect inmunofluorescence

Freshly prepared eGUVs were incubated for 1 h in isosmolar buffer solution containing primary monoclonal anti-human α,β-spectrin (anti-body final concentration, 4 μg/ml, 75 mM NaCl, 40 mM glucose, 10 mM Hepes, 1 mM $MgCl_2$, 1 mM KCl, pH = 7,4). The secondary fluorescent antibody Alexa Fluor 488 goat anti-mouse IgG, IgA, IgM (H + L) (ca. 4 μg/ml, final) was subsequently incubated for 1 h more. Actin staining was performed by adding 5 uL of Alexa Fluor® 594 Phaolloidin solution to 100 μL of eGUV suspension (80 μL + 20 μL of eGUV containing ATP (>1 mM final) when necessary) and incubated for 1 h.

2.6. Simultaneous fluorescence and AFM imaging in amplitude modulated dynamic mode (abbrev. AM)

100 μL of eGUV suspension (at different ATP concentration) were incubated on glass cover slides (Menzer-gläser, #2 Ø 24 mm) for 30 min. The hydrophilic interaction between the negative glass and erythrocyte membranes is mediated by the presence of divalent ions and resulted in the formation of supported membranes spread onto the glass surface. Prior to AFM visualization, the spread membranes were washed with abundant ATP containing buffer. AFM characterization of Figs. 2 and 5 was performed using a JPK NanoWizard II, coupled to a Nikon Eclipse Ti inverted fluorescence optical microscope. The AFM was operated in amplitude modulated dynamic mode in aqueous solution, an intermittent contact mode where the cantilever oscillates at its resonant frequency. Imaging is performed when a setpoint of amplitude is chosen, and the height adjusted to match this amplitude through the feedback system. Height, error, and phase signals were simultaneously recorded. The amplitude error signal is very sensitive to the in plane derivative of the topography whereas the phase is related to the energy dissipation. An Olympus commercial silicon nitride cantilever tip with a force constant of 0.76 N/m (calibrated by thermal tuning), 15 nm of nominal radius, and a free resonant frequency of 71 kHz was employed.

2.7. PeakForce tapping quantitative nanomechanical mapping AFM measurements (abbrev. PeakForce/PF-QNM)

ErythroGUV membranes were spread on glass coverslips by incubating vesicle suspensions at different ATP concentrations. In order to measure nanomechanical maps of the samples a Bruker Bioscope Catalyst AFM operating in PeakForce Tapping mode was used. Here the cantilever is excited by a Z piezo oscillating at 1 kHz, and the tip interacts with the sample every cycle at the lowest part of the oscillation. A topography image is built from the voltage applied to the Z piezo scanner so that the peak value of the force for each actuation cycle is kept constant along XY scanning. During this feedback adjustment of the peak force to a setpoint a finite error is introduced. As a result a peak-force error channel can be built, which is related to the derivative of the topography and its magnitude dependent on the sample stiffness. The peak-force setpoint was 1 nN and the amplitude of the piezo oscillation was set to 20 nm. All the measurements have been taken with the same probe: a Bruker^{TM} MLCT silicon cantilever with a stiffness of 0.94 N/m (calibrated by thermal tuning) and a tip of 50 nm of radius (measured by SEM, Fig. S1). Simultaneously to AFM imaging a quantitative nano-mechanical mapping is performed (PF-QNM mode). When the tip interacts with the sample, a force – vs- distance curve is collected and analyzed by the software. Local values of the apparent Young's modulus are extracted by fitting the force curves to the Hertz-model [29]. The fitting is performed inside a particular boundary of the contact region [30]. A minimum of 4% of the peak-force (setpoint + error) has been established as the origin of the force fitting region. Below this threshold, the noise level and the off-contact portions of the force curves forbid proper interpretation. On the other hand, and unless stated otherwise, the maximum force fitting boundary used was limited to 40% of the peak-force (setpoint + error), to exclude substrate stiffening artifacts. This criterion limits the indentation forces up to 300–500 pN, depending on the sample dependent peak-force error. Within Hertz model, the indentation force vs. indentation depth curve $F\left(\delta\right)$ is described as follows [31]:

$$F = 4ER^{1/2}\frac{\delta^{3/2}}{3\left(1-\nu^2\right)}, \quad (1)$$

where E is the apparent Young's modulus, R is the tip radius, and ν the Poisson ratio, chosen as 1/3 [32]. The fits were performed in a log–log representation, inside the indicated force boundary, resulting in a linear fitting with a 3/2 slope. The approach indentation curves were analyzed. The retract curves are equivalent to the extend ones for every sample, that is, there is no significant hysteresis of the tip-sample interaction cycle. Therefore, viscoelastic contributions at the frequency of perturbation (1 kHz), and/or artifacts like hydrodynamic damping and adhesion effects can be neglected. The resolution of the topography images and mechanical maps were of 256 × 256 pixels.

3. Results

3.1. Reconstruction of erythroid membrane skeletons

To prepare erythroid membrane skeleton composite microfilaments on artificial vesicles, erythroid membranes were purified from healthy human RBCs and then spread onto ITO cover slides for vesicle electro-swelling [28]. For a better visualization, erythroid membranes were labeled using a fluorescent lipid (rhodamine-phosphatidylethanolamine: Rho-PE) that was mixed with the erythroid extract prior to vesicle electroformation. Fluorescence microscopy shows that in the absence of ATP, giant vesicles display homogeneous fluorescence (see Fig. 1A). Upon the addition of ATP (>1 mM), a fluorescent network on the membrane surface formed instantaneously (Fig. 1B). To characterize the structural organization of the filaments at nanometric resolution, eGUVs were spread onto glass cover slides by fusion of the giant vesicles from a buffer suspension. When transferred to flat solid supports, the eGUVs tightly adhered to the glass slide because of their high hydrophilic interaction with this substrate (Fig. 1C–E). After substrate adhesion, vesicles explode from the apical pole, which becomes stressed beyond the rupture limit. The luminal side of the eGUVs is exposed face up and remains essentially unaltered, which allows further AFM characterization (Fig. 1F–I). These membranes will be referred to as spread membranes. Actin and spectrin are the elemental molecular bricks of the native membrane skeleton. In our case, it can be hypothesized that the observed microfilaments are composed by a hybrid assembly of polymerizing actin and spectrin oligomers. To confirm the nature of the protein filaments, eGUVs were incubated with monoclonal anti-spectrin antibodies and with the fluorescently labeled phalloidin to specifically stain spectrin (green channel) and filamentous actin or F-actin (red channel) respectively (Fig. 1C–E). Nonetheless, next to spectrin and actin the presence of other proteins cannot be discarded (see below).

3.2. Nanostructural characterization of protein networks

We first looked at spread membranes in the absence of ATP. A representative image for non-polymerized patches is shown in Fig. 2A (fluorescence) and 2 B (AFM). A detailed zoom, measured far from the flaws of the rupture process, evidences the presence of structures sizing in the nanometer range (Fig. 2C). In the absence of ATP, spread eGUVs displayed a protein background formed by a globular pool with sparse inclusions of larger blobs (30–40 nm size). A bimodal analysis of the height histogram reveals a dense relatively homogeneous background, with a typical height ca. 3 ± 2 nm, compared to the broader distribution of the larger blobs, spanning from 2 nm up to 14 nm in height (see Fig. 2D). These results are in agreement with previous AFM data [28] which revealed a similar size of the protein population at the luminal side of native membranes, where the majority of globular particles were assigned to Band 3 molecules [1]. The presence of millimolar concentration of ATP causes the membrane associated proteins to rearrange and progressively connect with each other to form a connected network of protein strands (Fig. 2E). At the microscale, the network appears to be strongly disordered and constituted by thick filaments of variable length (1–2 μm) joined at the nodes of the network (mostly, 3-fold linked), as visualized under the fluorescence microscope. AFM reveals a higher complexity in the nanoscale, where the network actually appears as complex structures made of tangled filaments (Fig. 2F). These complex strands are significantly larger (50–100 nm in height, Fig. 2H) than the single elements observed in the absence of ATP, suggesting a composite structure (see Fig. 2G). Unlike the dense pool of protein particles observed in the absence of ATP, no proteins are now visible in the spaces (lacuna patches) among the filaments in the network and suggests that these lacunar patches can be considered as a homogeneous lipid bilayer, in view of the low roughness (<1 nm, see Fig. 2H). This suggests that the entire protein pool on the membrane surface has been recruited to the stranded structure upon ATP incubation. Moreover, all the protein strands of the network appear fluorescently stained with the Rho-PE dye, implying a complex protein composition probably mixed with lipids (Rho-PE label and PE among them). The specific interaction of PE lipids with spectrin has been previously reported by others [33–35], thus the presence of rho-PE within the protein microfilaments indicates a localization of the dye through spectrin specific interactions.

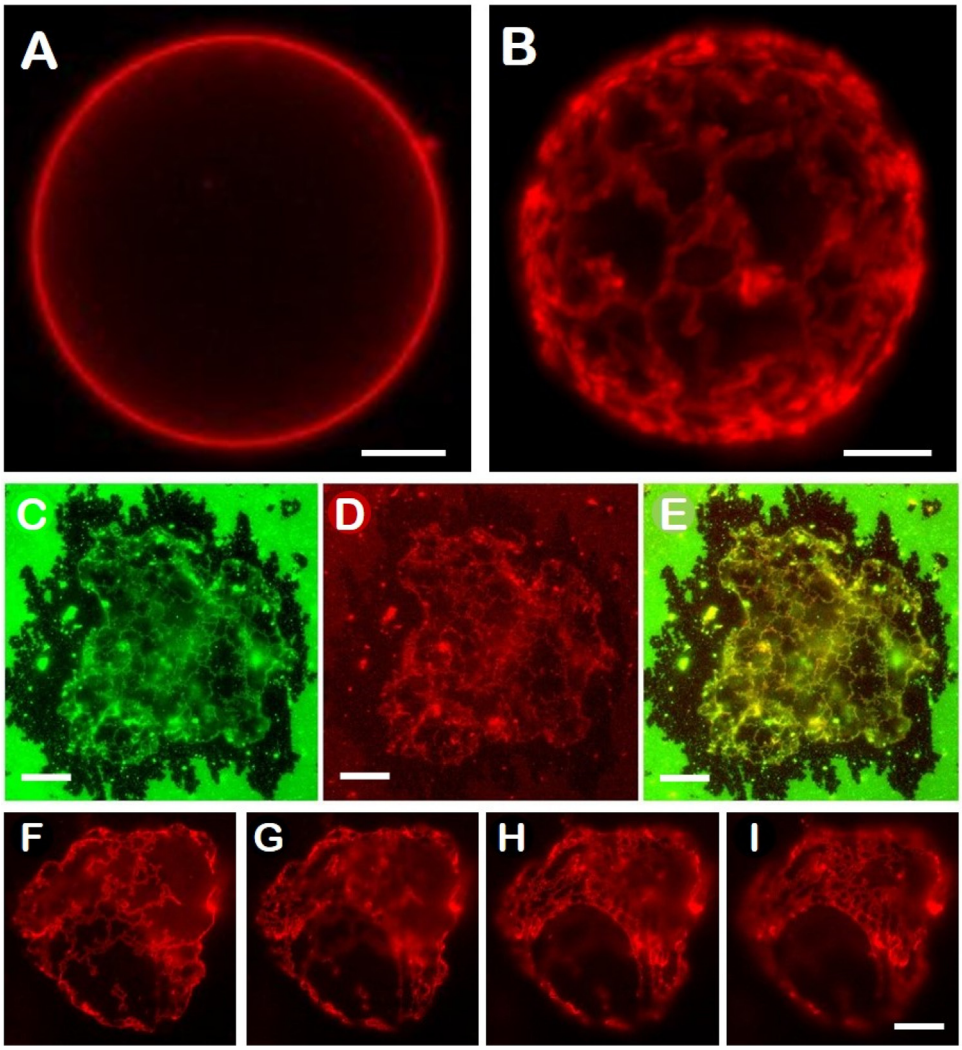

Fig. 1. (A) Fluorescence microscopy image (rho-PE fluorescence signal) of eGUVs in the absence of ATP and (**B**) in the presence of millimolar concentration of ATP. **(C–E)** Planar bottom transfer of a typical membrane skeleton stuck at the microscope cover slide. Immunofluorescence staining of collapsed eGUVs incubated with anti-spectrin antibodies (C, green) and fluorescent phalloidin (D, red). (E) Merged image of H and I. **(F–I)** eGUV glass slide collapse: Vesicles break from the top and expose luminal side of the vesicle, keeping the protein network facing up and remain properly oriented for AFM characterization. Images were captured at different focal planes with a z-step of 0.7 μm. Scale bars represent 10 micrometers. (For interpretation of the references to color in this figure legend, the reader is referred to the web version of this article.)

3.3. PeakForce tapping AFM measurements

To go one-step further beyond the topographical characterization, we discriminate the different protein structures by studying their mechanical properties. We have taken advantage of nanomechanical measurements by PeakForce tapping AFM (PF-QNM) to map the mechanical response of the eGUV membrane surface [36]. Fig. 3 shows typical indentation curves for the protein arrangements shown in Fig. 2. Indentation on globular or filamentous regions gives rise to different mechanical behavior. For example, in the absence of ATP (Fig. 3A), the curves on the globular protein background are steeper than the curves corresponding to the larger blobs (Fig. 3B). An important artifact related to the indentation is the overestimation of the sample stiffness by the presence of the underlying rigid glass substrate. To discriminate the substrate effect, the Young's modulus is calculated as a function of the indentation force; this can be done by fitting progressively the force curves to wider force ranges. The substrate-stiffening artifact is present clearly beyond 0.4 nN (Fig. 3C), where the elastic modulus is not constant anymore and starts to raise with the indentation force. According to this behavior and, to get reliable elastic modulus maps intrinsic to the sample, we have restricted the fitting region of the indentation curves up to 40% of the peak-force (see Methods). In the presence of ATP (Fig. 3D), two different regions can be distinguished according to the mechanical response (Fig. 3E): the flat and rigid lipid patches that are characterized by very steep force-vs-distance curves (red open circles), and the protein network, with a shallow curve (blue open circles). Furthermore, the different slopes obtained from the different components of the protein network (Fig. 3E) reveal the mechanical heterogeneity of the composite filaments. The Young's moduli from the indentation curves are shown in Fig. 3F. Here, two remarkable effects can be observed. First, the substrate artifact is not significant up to 40–50% of the peak-force, even for the lipid bilayer corresponding to a thickness of a few nanometers.

3.4. Nanomechanical characterization

The PF-QNM mode allows the analysis, in real time, of the indentation curves recorded for each point of the AFM image by fitting them to the Hertz model. The mechanical maps can be plotted as the fitted values of the Young's modulus (see Methods). Fig. 4 shows the mechanical maps corresponding to Fig. 3. The topographical image (Fig. 4A) nicely correlates with the nano-

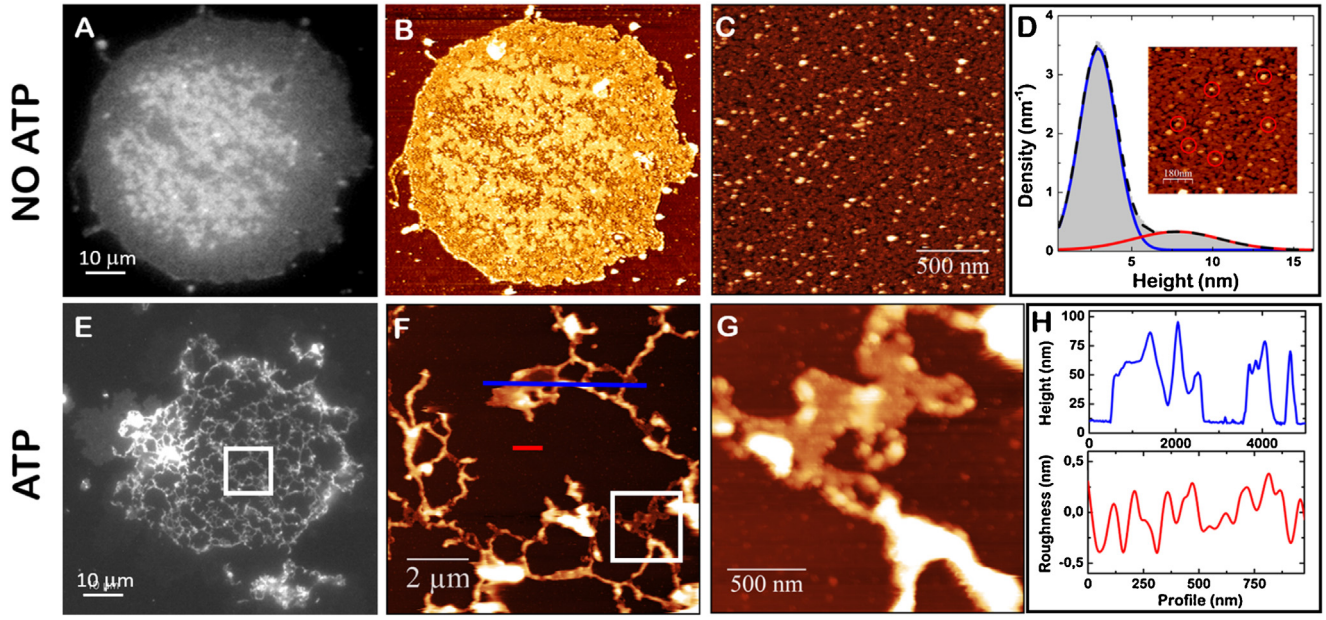

Fig. 2. **(A)** Fluorescence image of a Rho-PE stained collapsed eGUV spread onto a mica substrate in the absence of ATP. **(B)** AFM topography image of the same vesicle (AM mode) in (A). **(C)** Detailed AFM topography of a supported eGUV membrane. **(D)** Height histogram of C. **Inset:** Some 8–10 nm blobs are highlighted in red circles. **(E)** Fluorescence image of a Rho-PE stained collapsed eGUV membrane spread onto a mica substrate in the presence of ATP (showing the formed protein network). **(F)** AFM topography image of the framed zone in (E). **(G)** AFM topography image of the framed zone in (F). **(H)** Height profile (blue) of a representative protein microfilament in (F) and the roughness profile (red) of the underlying bilayer. (For interpretation of the references to color in this figure legend, the reader is referred to the web version of this article.)

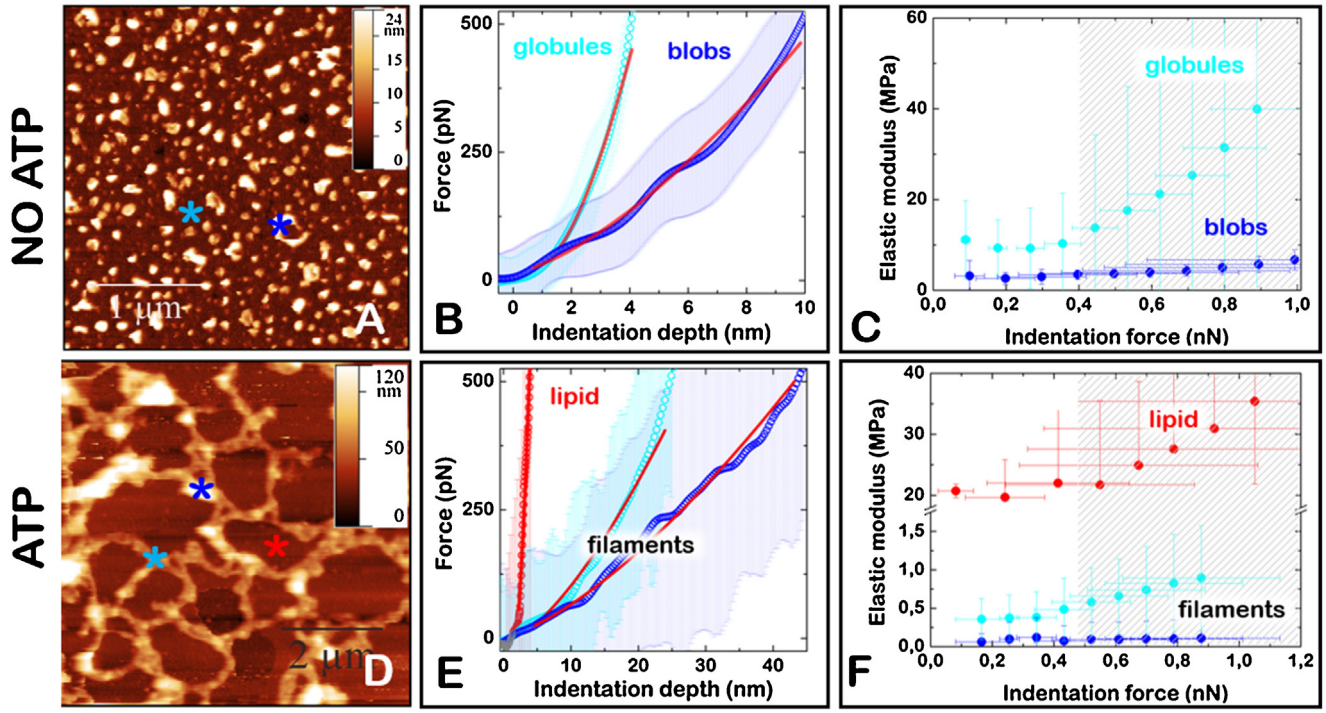

Fig. 3. **(A)** AFM topography image of a spread eGUV in the absence of ATP. **(B)** Force curves (symbols) taken on the regions indicated by the blue stars (average of an ensemble of 30 forces curves sample with standard deviations given by the error bars). The continuous lines are fittings to Eq. (1) **(C)** Dependence of the elastic modulus with the indentation force as obtained from the indentation curves shown in B. Each point represents the average of the Young's modulus resulting from fitting the 30 force curves of the regions marked in A and B, in wider force fitting boundaries (standard deviations as error bars). The first range is limited up to 20% of the peak-force, and a cumulative 10% has been added for subsequent ranges. **(D)** AFM topography image of a spread eGUV in the presence of 1 mM ATP. **(E)** Force curves (symbols) taken on the regions indicated by blue and red stars (average of a sample of 30 forces curves with standard deviations given by the error bars). The continuous lines are fittings to Eq. (1) **(F)**. Dependence of the elastic modulus with the indentation force as obtained from the indentation curves shown in E. Each point represents the average of the Young's modulus resulting from fitting the 30 force curves of the regions marked in D–E in wider force fitting boundaries (standard deviations as error bars). The first range is limited up to 20% of the peak-force, and a cumulative 10% has been added for subsequent ranges. A minimum of 4% of the peak-force has been established as the origin of the force fitting region. (For interpretation of the references to color in this figure legend, the reader is referred to the web version of this article.)

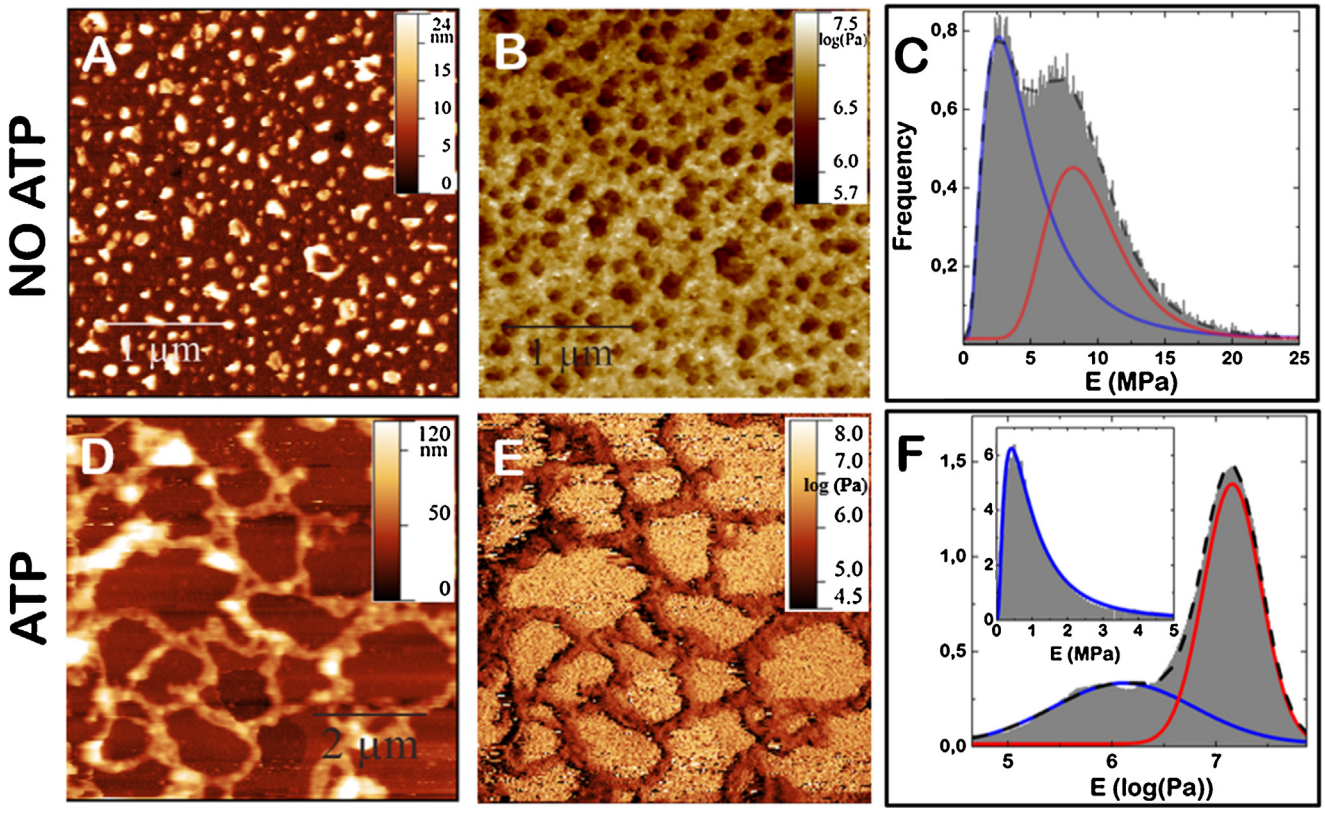

Fig. 4. **(A)** AFM topography of a supported eGUV in the absence of ATP. (B) Young's Modulus map of (A) as obtained by PF-QNM. **(C)** Histogram of the Young modulus values shown in (B). Two lognormal distributions describe the mechanical modulus of the two distinctive structural populations: blobs and globules. **(D)** AFM topography of a supported eGUV in the presence of 1 mM ATP. **(E)** Young's Modulus map of (D) as obtained by PF-QNM. **(F)** Histogram (log scale) of the Young modulus values shown in (E). Two lognormal distributions describe the mechanical modulus of the two distinctive structural populations: lipid patches and protein composite filaments. The inset shows the histogram of the Young modulus values for the protein network.

mechanical map (Fig. 4B) of the eGUV in the absence of ATP. As shown previously, the sample shows dispersed protein particles on a homogeneous dense protein rich background layer. The quantitative analysis of the mechanical map (Fig. 4C) reveals a bimodal distribution with the softer component corresponding to the larger blob particles, and the stiffer component corresponding to the globular proteins in the background. To accurately determine averaged values of the mechanical modulus corresponding to the two structurally-differentiated species, the distribution of Young's moduli is analyzed by decomposition into several contributions. The best fit requires two lognormal components with average and standard deviations, $E_{blob} = 4 \pm 3$ MPa and $E_{glob} = 9 \pm 3$ MPa respectively. This assigns the larger protein assemblies a relatively softer character than the surrounding globular protein. Fig. 4 also contains typical AFM images (4D: topographical and 4E: mechanical) of the protein network formed in the presence of ATP. As expected from the indentation curves (Fig. 3E), the lipid patches are found to be stiffer than the protein filaments. A bimodal analysis of the distribution reveals overlapped populations, which are characterized by two size distributions, corresponding to protein filaments and lipid patches (Fig. 4E) respectively. The flat patches are characterized by a high value of the apparent Young's modulus, 20 ± 8 MPa, in agreement with the reported values for lipid bilayers [37]. A broad distribution centered at a low value of the Young's modulus that can be assigned to the protein network is observed upon analysis of the mechanical map (Fig. 4F). In order to map the elasticity of the protein network, we have masked the lower level of the AFM images (heights lower than 35 nm were hidden in the stiffness map). The averaged value of the Young modulus of the filamentous strands is found at $E_{fil} = 0.4 \pm 1.5$ MPa. The large deviation reflects heterogeneous elasticity with values ranging from a few hundred kPa up to few MPa (see inset in Fig. 4F). On average, the protein filaments that form the network strands are characterized by a relatively low mechanical modulus with an order of magnitude lower than the protein assemblies ($E_{blob} = 4$ MPa) observed in the non-polymerized background (Fig. 4C). This trend indicates a softening of the protein microfilaments, which is promoted by protein clustering occurred upon the addition of ATP.

4. Discussion

4.1. Mechanical imaging of lipid-protein layers

The required prerequisites to image heterogeneous samples of soft matter primarily deal with conditions to probe elastic response in the linear regime by AFM techniques, while minimizing the invasion of the AFM tip in the sample structure [38]. We have tried to minimize the working force/amplitude within our AFM set-up and, at the same time, getting robust results (*i.e.* stable behavior of the real-time indentation curves). In general, to fit the force curves we considered maximum forces of 500 pN, corresponding to typical indentations of 20 nm depth (see Methods and Results section). Even though these conditions represent one order of magnitude above previously reported conditions [27], we have confirmed that the Hertz model [29], a contact model within the linear theory of elasticity, describes adequately the force curves. Furthermore, the Hertz models holds with a related elastic modulus which is indentation independent. In the literature, different corrections to Hertz-Sneddon models have been proposed to account for artificial stiffening of a finite layer when compressed against a

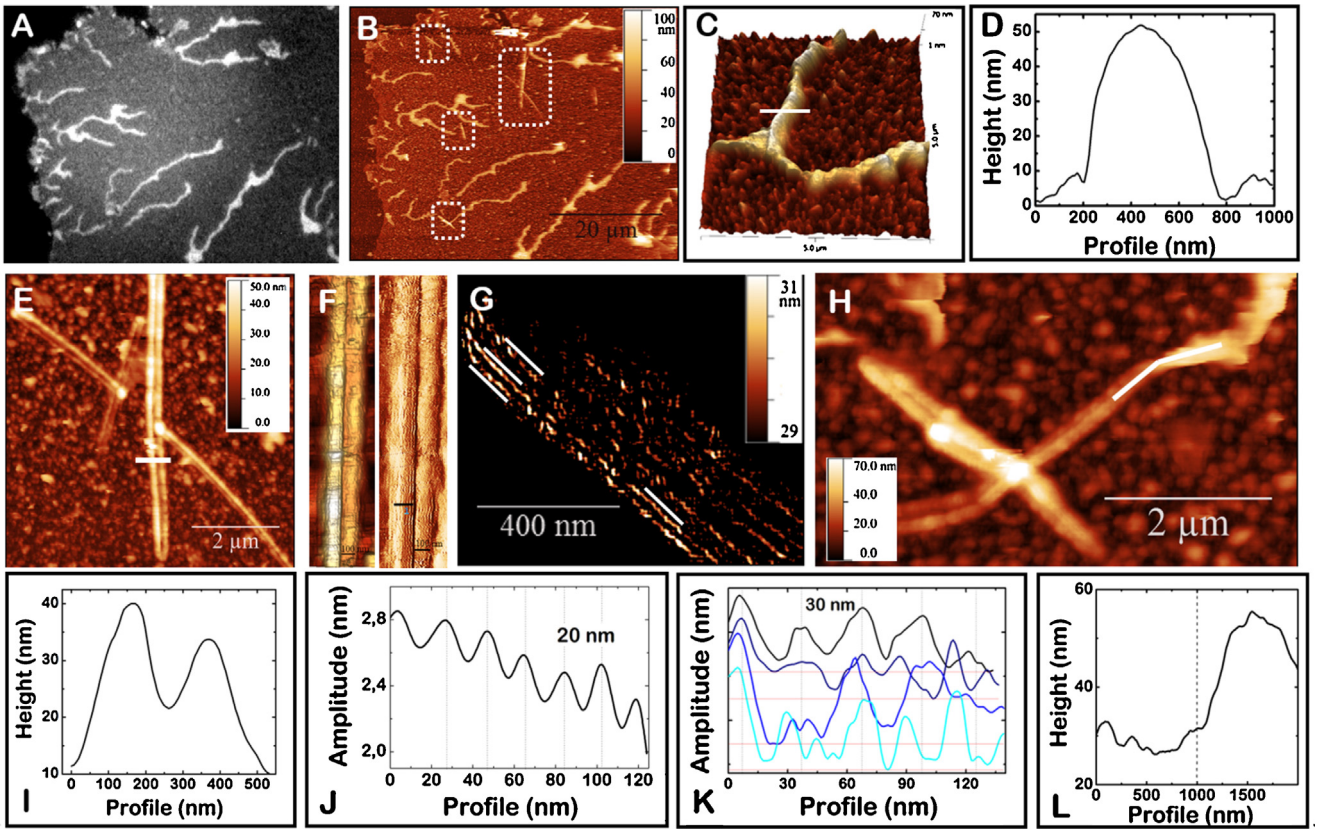

Fig. 5. **(A)** Fluorescence image of a supported eGUV in the presence of submillimolar concentration of ATP and as stained by Rho-PE. **(B)** AFM Topography image of the same region shown in (A).White frames show several straight filaments that are unstained by Rho-PE. **(C)** 3D AFM topography image of a sinuous filament. **(D)**. Transversal profile of the filament shown in (C). **(E)** Detailed AFM topography image of a straight filament framed in (B). **(F)** Detailed view of the straight filament shown in (E) in topographic (left) and amplitude (right) channels. **(G)** Detail of a straight filament ending as shown in the amplitude channel of (E). The image has been processed by a contour-detection algorithm to highlight the superficial filaments (the rest of the image has been masked out). **(H)** AFM topography image of straight filaments connected to a sinuous filament. **(I)** Transversal profile of the straight double filament shown in (E). **(J)** Transversal profile of the bundled protofilaments shown in (F). **(K)** Longitudinal profiles of bundled filaments as measured on the amplitude channel in (G). **(L)** Height profile of the straight-sinuous filaments junction.

rigid substrate, *e.g.* adding terms in powers of relative deformation (indentation depth/sample thickness) [31,39]. We adopted here a more empirical approach. We have used the bare Hertz model, without corrections, and determined the experimental conditions where the modulus is independent of indentation parameters. For convenience, we chose force as a measure of the indentation rate instead of relative deformation. Whereas the indentation force is directly obtained from the force curve information, the relative deformation is calculated with the additional input of the sample thickness. For every sample tested in this work, the Hertz elastic modulus is constant up to indentation forces of around 300–500 pN, with modulus in the range of 0.1–20 MPa. We have set up the experimental conditions where PF-QNM measurements provide intrinsic linear mechanical properties of thin protein-lipid composite layers of the studied biological system.

4.2. Network structure

From the results, an open question emerges about how the protein network is formed. Arguably, among other possible self-assembly driving mechanisms, protein filament formation might be attributed to a partial denaturation after pH drop (down to pH 5) by the addition of non-buffered ATP to vesicles. This acidity might trigger the observed protein aggregation [40], although it does not explain itself protein polymerization/clustering into reticular structures. The cytosolic ATP hydrolyzing enzyme (ATPase) actin is the only polymerizing protein in the native erythroid and the eGUV cytoskeleton (see Fig. 1). Upon the binding of ATP, actin assembles into long protein filaments (F-actin) and disassemble back to the monomeric globular state (G-actin) once the bound ATP has been hydrolysed and eventually released as ADP and inorganic phosphate (P_i). This dynamic assembly cycle allows the rapid remodeling of the filament and quick-change of the cellular structure and shape in response to an environmental stimulus. To unveil how actin may have a possible scaffolding role in network formation, a structural analysis was performed by incubating eGUVs with low concentration of unbuffered ATP (0.1 mM), that is sufficient to trigger actin polymerization cycle but does not change the pH of the sample. At these submillimolar ATP conditions, Rho-PE staining revealed the presence of PE-associated filaments with a sinuous river-like contour streaming-out from the center of the membrane patches toward the outer rim (see Fig. 5A). Detailed AFM-topography zooms do not reveal defined ultrastructure inside such filaments (see Fig. 5B and C), which appear rather organized as a heterogeneous wire with multiple branching. They rest over the sea of globular particles that were observed in the absence of ATP, which appear undisturbed by the presence of the filaments (see Fig. 5C). These filaments are sinuous, multiply branched and characterized by a variable length and a near constant thickness ca. 50 ± 10 nm (Fig. 5D), thus probably constituted by the oligomerization of spectrin-based bundles with other protein building blocks. Additionally, straight highly persistent filaments are also observed by AFM imaging (see boxes in Fig. 5B). Unlike the sinuous filaments, these straight filaments are not visible under fluorescent staining with Rho-PE, which discards the presence of flexible spectrin within these persistent filaments. A detailed topographic analysis

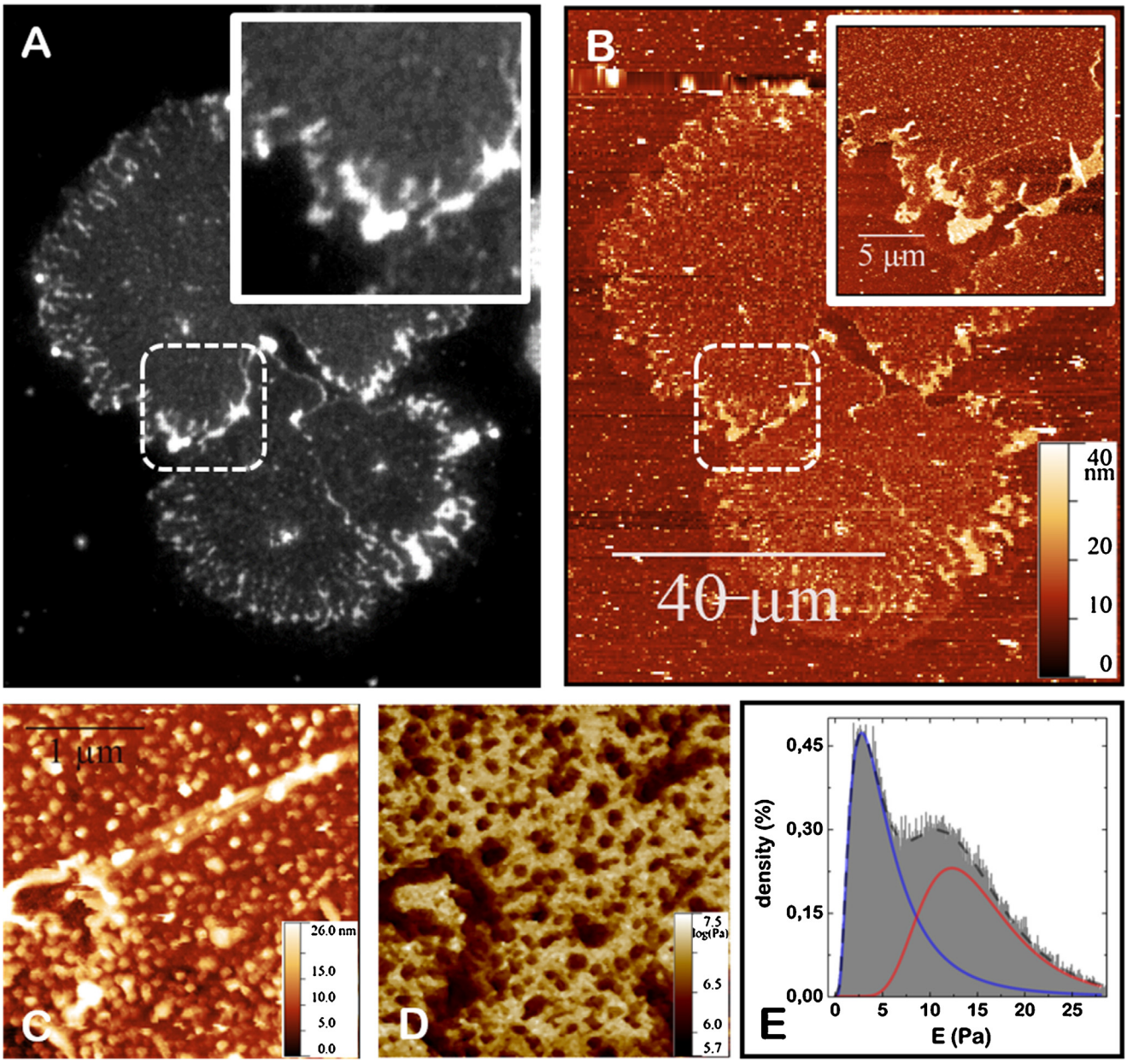

Fig. 6. **(A)** Fluorescence image of a supported Rho-PE stained eGUV at low ATP concentration. **(B)** AFM topography image of the same vesicle shown in A. The insets show a region where an unstained actin-enriched filament was detected by AFM. **(C)** AFM topography view of the actin-enriched filament linked together to a sinuous filament. **(D)** PF-QNM Young modulus map of (C). **(E)** Young modulus histogram of D. The two lognormal distributions describe the modulus of the two distinctive structural populations shown in (C) and (D): globules and actin-enriched filaments and blebs and sinuous filaments.

shows that these straight filaments are relatively flat and organize as ribbon-pairs constituted by two parallel filaments laterally stuck together along the whole contour (see Fig. 5E). Every single filament is 150 ± 50 nm wide and 30 ± 10 nm high (Fig. 5I). More detailed structural information can be obtained by the amplitude channel images, *i.e.* the error signal, related to the derivative of the topography (see Experimental Section). Inspecting this channel, the ultrastructure of these straight ribbons is resolved as flat bundles composed of thinner proto-filaments, typically 8–10 parallel fibrils, equally spaced at $l_{\perp} = 20 \pm 4$ nm as seen in Fig. 5F and J (see Fig. S2 for similar examples). In the amplitude channel, a repetitive spacing is also detected along the longitudinal axis of each single protofilament $l_{\parallel} = 30 \pm 5$ nm (see Fig. 5G and K). As actin is the only protein of the erythrocyte cytoskeleton network molecule that is able to polymerize into proto-filaments and the observed straight ribbons are compatible with the dimensions of the helical F-actin proto-filaments (7 nm width, 36 nm helical pitch) [5], we hypothesize that at low ATP concentrations, F-actin-based ribbons of several micrometers in length can be resolved on the surface of eGUV membranes. In this artificial construction, unlike the native membrane where F-actin is capped as short filaments by the regulatory action of tropomodulin and/or adducin [41], the actin-based ribbons might lack the capping proteins, probably lost during membrane extraction or GUV electroformation. Both types of filaments, sinuous filaments based on flexible spectrin and straight ribbons based on actin, appear frequently fused together at hybrid junctions where a spectrin ribbon distally joins with the end of an actin-based filament (Fig. 5H). Although no deeper structural resolution of these hybrid junctions was possible, the smooth transition observed along the junction (Fig. 5L) suggests a direct spectrin-actin interaction playing a stabilizing role [42,43]. Arguably, actin polymers could be working as a rigid scaffold for spectrin networking, form-

ing a compacted actin-spectrin structure compatible with spectrin bundling. Although the image resolution of our AFM images is comparable to published transmission electron microscopy images of erythrocyte membranes [44], we plan to use a combination of biochemistry, scanning and transmission electron microscopy in the near future to understand the nature of the proteins and their nanoscale interactions present in our spread eGUV membrane.

To discuss the complexity of the network in regard to its local elasticity, Fig. 6 shows a set of fluorescence (Fig. 6A), AFM topographical (Fig. 6B and C) and mechanical (Fig. 6D) images that correspond to the same membrane patch spread onto a glass surface in the presence of low ATP concentration (0.1 mM). Two classes of filaments are identified by RhoPE fluorescence and AFM topography respectively (see Fig. 6A and B). Furthermore, these two structural classes also endow mechanical differences. Fig. 6 shows sinuous filaments principally made of flexible spectrin as revealed by Rho-PE. Also, rigid filaments principally made of actin are also present, although they are only visible in the AFM image (see Fig. 6A and B). Fig. 6C and D show the structure-mechanical map of the zoomed region that contains both, sinuous and straight filaments, in coexistence with non-polymerized protein pool. The sinuous filament in the left side of Fig. 6C (15–20 nm thick) is also found in Fig. 6D, with a similar mechanical response than the single blobs shown in Fig. 4. However, the double straight filament in the middle of the topographic image (Fig. 6C) is undistinguishable from the lipid-protein background which appears stiffer than the protein blobs in the mechanical image (Fig. 6D). From the analysis of the mechanical modulus histogram of Fig. 6E, the sinuous filaments are characterized by a Young's modulus, $E_{sin} = 5 \pm 4$ MPa, which is similar to that corresponding to the discrete blobs. In contrast, the straight filaments have a high mechanical stiffness, $E_{str} = 15 \pm 4$ MPa, similar to the values measured for the surrounding globular protein sea. Similar pictures are shown in Fig. S3. It must be stressed that the composite strands of the protein network found at mM ATP concentration have different mechanical properties than the nascent individual filaments found at low ATP concentration. Either sinuous filaments or actin-enriched filaments are stiffer (5–15 MPa) than the composite strands (0.5 MPa). This observation is in agreement with previous results of spectrin mechanics in experiments carried out in the absence of cytosolic kinases, which report a spectrin softening upon phosphorylation [45].

4.3. Mechanostructure and functional mechanics

The stability of the erythrocyte membrane and its mechanical function are both directly related not only with their microscopic organization of the cytoskeleton at a subcellular scale but also with the nanoscopic elasticity of its single components. Indeed, changes in the membrane affinity of the spectrin and actin filaments have been reported to correlate with significant changes in the stiffness of Sickle Cell Trait erythrocytes [5]. Similar observations have been reported in other pathological erythrocytes [7], or in erythrocytes affected by biochemical agents, e.g. an increased concentration of Ca^{+2} results in higher cytoskeleton rigidity via an increased binding of band 3 to the spectrin bound ankyrin [17]. Also, venom toxins produce cytoskeleton protein reorganizations that trigger membrane stiffening [24]. In our case, the protein composite filaments that form the network are soft in terms of Young's modulus as compared with the non-polymerized single protein components. In the microscale, the soft composite strands are able to produce a stiffer network that supports rigidity in terms of structural shear and bending deformations, as previously reported [22]. This is not paradoxical, as the network itself is able to build in the microscale a lower resilience than the individual filaments [46]. Consequently, the protein filaments allow large deformations at the nanoscale, whereas the network supports a high structural rigidity. Otherwise said, the supramolecular assembly is structurally rigid in the global scale but allows small local changes to accommodate membrane deformability. This observation might be relevant for understanding the mechanism thereby pathological erythrocytes are intrinsically stiffer than healthy ones [47].

5. Conclusion

We have shown that a composite protein network can be reconstructed on giant unilamelar vesicles fabricated from erythroid native membranes, eGUVs. eGUVs were spread onto mica surface to form supported layers for AFM characterization. Using AFM both in Amplitude Modulated and Peak Force modulated dynamic modes, we have imaged the individual filaments forming the protein network. Peak Force Quantitative Nanomechanical Measurements have been analyzed within properly defined force boundaries in order to avoid artifact stiffening. They revealed nanomechanical differences between the non-polymerized proteins and the composite filaments. In the absence of ATP, the globular protein pool is characterized by Young's moduli of several MPa, whereas the network is formed by much softer composite strands (hundreds of kPa). Although the nanostructured components forming the protein microfilaments are relatively compliant, their structural assembly as a topological network causes additional rigidification in the microscale. The reported protein rearrangement could be relevant for understanding the mechanisms of the described membrane stiffening of pathological erythrocytes.

Acknowledgments

This work was supported by the ERC Starting Grant "mitochon" (ERC-StG-2013-883188) and "Programa Ramon y Cajal" (RYC-2013-12609) from the Spanish Ministry of Economy MINECO (I. L-M.), the ERC Starting Grant "NANOFORCELLS" (ERC-StG-2011-278860) (M. E., A. C-M., M. C.), the project FORCE-for-FUTURE (CSD2010-00024) (A. S. P.) and FIS2012-35723 from MINECO (F.M.). M.E. wants to acknowledge Dr. Valerio Pini for his technical assistance during the SEM measurements.

Appendix A. Supplementary data

Supplementary data associated with this article can be found, in the online version, at http://dx.doi.org/10.1016/j.colsurfb.2016.10.022.

References

[1] Y. Yawata, Cell Membrane: The Red Blood Cell as a Model, Wiley-VCH Weinheim, 2003.
[2] J.S. Morrow, V.T. Marchesi, Self-assembly of spectrin oligomers invitro – a basis for a dynamic cytoskeleton, J. Cell Biol. 88 (1981) 463–468.
[3] J.A. Ursitti, V.M. Fowler, Immunolocalization of tropomodulin, tropomyosin and actin in spread human erythrocyte skeletons, J. Cell Sci. 107 (1994) 1633–1639.
[4] A. Nans, N. Mohandas, D.L. Stokes, Native ultrastructure of the red cell cytoskeleton by cryo-electron tomography, Biophys. J. 101 (2011) 2341–2350.
[5] A. Tamura, T. Sato, T. Fuji, Study of the shape transformation of human erythrocytes, in: S.T. Ohnishi, T. Ohnishi (Eds.), Membrane Abnormalities in Sickle Cell Disease and in Other Red Blood Cell Disorders-CRC Series in Membrane-Linked Diseases, CRC Press, London, 1994, pp. 245–268.
[6] W. Malorni, F. Iosi, G. Donelli, P. Caprari, A.M. Salvati, P. Cianciulli, A new, striking morphologic feature for the human erythrocyte in hereditary spherocytosis – the blebbing pattern, Blood 81 (1993) 2821–2822.
[7] W. Malorni, E. Straface, G. Pagano, D. Monti, A. Zatterale, D. Del Principe, I.B. Deeva, C. Franceschi, R. Masella, L.G. Korkina, Cytoskeleton alterations of erythrocytes from patients with Fanconi's anemia, FEBS Lett. 468 (2000) 125–128.
[8] M. Takeuchi, H. Miyamoto, Y. Sako, H. Komizu, A. Kusumi, Structure of the erythrocyte membrane skeleton as observed by atomic force microscopy, Biophys. J. 74 (1998) 2171–2183.

[9] S. Yamashina, O. Katsumata, Structural analysis of red blood cell membrane with an atomic force microscope, J. Electron Microsc. 49 (2000) 445–451.
[10] A.H. Swihart, J.M. Mikrut, J.B. Ketterson, R.C. MacDonald, Atomic force microscopy of the erythrocyte membrane skeleton, J. Microsc.-Oxford 204 (2001) 212–225.
[11] D.J. Muller, AFM: a nanotool in membrane biology, Biochemistry-US 47 (2008) 7986–7998.
[12] T. Ando, T. Uchihashi, S. Scheuring, Filming biomolecular processes by high-speed atomic force microscopy, Chem. Rev. 114 (2014) 3120–3188.
[13] F. Liu, J. Burgess, H. Mizukami, A. Ostafin, Sample preparation and imaging of erythrocyte cytoskeleton with the atomic force microscopy, Cell Biochem. Biophys. 38 (2003) 251–270.
[14] R. Nowakowski, P. Luckham, P. Winlove, Imaging erythrocytes under physiological conditions by atomic force microscopy, BBA: Biomembranes 1514 (2001) 170–176.
[15] H.D. Wang, X. Hao, Y.P. Shan, J.G. Jiang, M.J. Cai, X. Shang, Preparation of cell membranes for high resolution imaging by AFM, Ultramicroscopy 110 (2010) 305–312.
[16] L. Picas, F. Rico, M. Deforet, S. Scheuring, Structural and mechanical heterogeneity of the erythrocyte membrane reveals hallmarks of membrane stability, ACS Nano 7 (2013) 1054–1063.
[17] F. Liu, H. Mizukami, S. Sarnaik, A. Ostafin, Calcium-dependent human erythrocyte cytoskeleton stability analysis through atomic force microscopy, J. Struct. Biol. 150 (2005) 200–210.
[18] M.N. Starodubtseva, T.G. Kuznetsova, S.A. Chizhik, N.I. Yegorenkov, Atomic force microscopy observation of peroxynitrite-induced erythrocyte cytoskeleton reorganization, Micron 38 (2007) 782–786.
[19] F. Liu, A.A. Khan, A.H. Chishti, A.E. Ostafin, Atomic force microscopy demonstration of cytoskeleton instability in mouse erythrocytes with dematin-headpiece and beta-adducin deficiency, Scanning 33 (2011) 426–436.
[20] H. Shi, Z. Liu, A. Li, J. Yin, A.G.L. Chong, K.S.W. Tan, Y. Zhang, C.T. Lim, Life cycle-dependent cytoskeletal modifications in plasmodium falciparum infected erythrocytes, PLoS One 8 (2013).
[21] Y.F. Dufrene, D. Martinez-Martin, I. Medalsy, D. Alsteens, D.J. Muller, Multiparametric imaging of biological systems by force-distance curve-based AFM, Nat. Methods 10 (2013) 847–854.
[22] S. Sharma, E.E. Grintsevich, M.L. Phillips, E. Reisler, J.K. Gimzewski, Atomic force microscopy reveals drebrin induced remodeling of F-actin with subnanometer resolution, Nano Lett. 11 (2011) 825–827.
[23] I. Lopez-Montero, R. Rodriguez-Garcia, F. Monroy, Artificial spectrin shells reconstituted on giant vesicles, J. Phys. Chem Lett. 3 (2012) 1583–1588.
[24] T.W. Yau, R.P. Kuchel, J.M.S. Koh, D. Szekely, P.J. Mirtschin, P.W. Kuchel, Cytoskeletal rearrangements in human red blood cells induced by snake venoms: light microscopy of shapes and NMR studies of membrane function, Cell Biol. Int. 36 (2012) 87–97.
[25] M.G. Millholland, R. Chandramohanadas, A. Pizzarro, A. Wehr, H. Shi, C. Darling, C.T. Lim, D.C. Greenbaum, The malaria parasite progressively dismantles the host erythrocyte cytoskeleton for efficient egress, Mol. Cell. Proteomics 10 (2011).
[26] T.L. Steck, J.A. Kant, Preparation of impermeable ghosts and inside-out vesicles from human erythrocyte membranes, Methods Enzymol. 31 (1974) 172–180.
[27] G.W. Burton, K.U. Ingold, K.E. Thompson, An improved procedure for the isolation of ghost membranes from human red blood cells, Lipids 16 (1981) 946.
[28] L. Mathivet, S. Cribier, P.F. Devaux, Shape change and physical properties of giant phospholipid vesicles prepared in the presence of an AC electric field, Biophys. J. 70 (1996) 1112–1121.
[29] H. Hertz, Ueber die berührung fester elastischer Körper, Journal für die reine und angewandte Mathematik (Crelle's Journal) 1882 (2009) s1.
[30] A. Calzado-Martin, M. Encinar, J. Tamayo, M. Calleja, A.S. Paulo, Effect of actin organization on the stiffness of living breast cancer cells revealed by peak-force modulation atomic force microscopy, ACS Nano 10 (2016) 3365–3374.
[31] E.K. Dimitriadis, F. Horkay, J. Maresca, B. Kachar, R.S. Chadwick, Determination of elastic moduli of thin layers of soft material using the atomic force microscope, Biophys. J. 82 (2002) 2798–2810.
[32] J. Li, M. Dao, C.T. Lim, S. Suresh, Spectrin-level modeling of the cytoskeleton and optical tweezers stretching of the erythrocyte, Biophys. J. 88 (2005) 3707–3719.
[33] A.F. Sikorski, K. Michalak, M. Bobrowska, Interaction of spectrin with phospholipids – quenching of spectrin intrinsic fluorescence by phospholipid suspensions, Biochim. Biophys. Acta 904 (1987) 55–60.
[34] A. Hryniewicz-Jankowska, E. Bok, P. Dubielecka, A. Chorzalska, W. Diakowski, A. Jezierski, M. Lisowski, A.F. Sikorski, Mapping of an ankyrin-sensitive, phosphatidylethanolamine/phosphatidylcholine mono- and bi-layer binding site in erythroid beta-spectrin, Biochem. J. 382 (2004) 677–685.
[35] X.L. An, X.H. Guo, H. Sum, J. Morrow, W. Gratzer, N. Mohandas, Phosphatidylserine binding sites in erythroid spectrin: location and implications for membrane stability, Biochemistry-US 43 (2004) 310–315.
[36] B. Foster, New atomic force microscopy (AFM) approaches life sciences gently, quantitatively, and correlatively, Am. Lab. 44 (2012) 24-+.
[37] I. Mey, M. Stephan, E.K. Schmitt, M.M. Muller, M. Ben Amar, C. Steinem, A. Janshoff, Local membrane mechanics of pore-spanning bilayers, J. Am. Chem. Soc. 131 (2009) 7031–7039.
[38] A.F. Payam, J.R. Ramos, R. Garcia, Molecular and nanoscale compositional contrast of soft matter in liquid: interplay between elastic and dissipative interactions, ACS Nano 6 (2012) 4663–4670.
[39] N. Gavara, R.S. Chadwick, Determination of the elastic moduli of thin samples and adherent cells using conical atomic force microscope tips, Nat. Nanotechnol. 7 (2012) 733–736.
[40] Y. Takakuwa, Regulation of red cell membrane protein interactions: implications for red cell function, Curr. Opin. Hematol. 8 (2001) 80–84.
[41] N. Mohandas, P.G. Gallagher, Red cell membrane: past, present, and future, Blood 112 (2008) 3939–3948.
[42] X. An, G. Debnath, X. Guo, S. Liu, S.E. Lux, A. Baines, W. Gratzer, N. Mohandas, Identification and functional characterization of protein 4.1R and actin-binding sites in erythrocyte beta spectrin: regulation of the interactions by phosphatidylinositol-4,5-bisphosphate, Biochemistry-US 44 (2005) 10681–10688.
[43] V. Ohanian, L.C. Wolfe, K.M. John, J.C. Pinder, S.E. Lux, W.B. Gratzer, Analysis of the ternary interaction of the red cell membrane skeletal proteins spectrin, actin, and 4.1, Biochemistry-US 23 (1984) 4416–4420.
[44] S. Tsukita, S. Tsukita, H. Ishikawa, S. Sato, M. Nakao, Electron-microscopic study of reassociation of spectrin and actin with the human-erythrocyte membrane, J. Cell Biol. 90 (1981) 70–77.
[45] S. Manno, Y. Takakuwa, K. Nagao, N. Mohandas, Modulation of erythrocyte-membrane mechanical function by beta-spectrin phosphorylation and dephosphorylation, J. Biol. Chem. 270 (1995) 5659–5665.
[46] D.H. Boal, Mechanics of the Cell, 2nd ed., Cambridge University Press, Cambridge, New York, 2012.
[47] R. Rodriguez-Garcia, I. Lopez-Montero, M. Mell, G. Egea, N.S. Gov, F. Monroy, Direct cytoskeleton forces cause membrane softening in red blood cells, Biophys. J. 108 (2015) 2794–2806.